

## Flight path planning in a turbulent wind environment

Fechner, Uwe; Schmehl, Roland

**DOI**

[10.1007/978-981-10-1947-0\\_15](https://doi.org/10.1007/978-981-10-1947-0_15)

**Publication date**

2018

**Document Version**

Final published version

**Published in**

Airborne Wind Energy

**Citation (APA)**

Fechner, U., & Schmehl, R. (2018). Flight path planning in a turbulent wind environment. In R. Schmehl (Ed.), *Airborne Wind Energy: Advances in Technology Development* (pp. 361-390). (Green Energy and Technology; No. 9789811019463). Springer. [https://doi.org/10.1007/978-981-10-1947-0\\_15](https://doi.org/10.1007/978-981-10-1947-0_15)

**Important note**

To cite this publication, please use the final published version (if applicable). Please check the document version above.

**Copyright**

Other than for strictly personal use, it is not permitted to download, forward or distribute the text or part of it, without the consent of the author(s) and/or copyright holder(s), unless the work is under an open content license such as Creative Commons.

**Takedown policy**

Please contact us and provide details if you believe this document breaches copyrights. We will remove access to the work immediately and investigate your claim.

***Green Open Access added to TU Delft Institutional Repository***

***'You share, we take care!' – Taverne project***

**<https://www.openaccess.nl/en/you-share-we-take-care>**

Otherwise as indicated in the copyright section: the publisher is the copyright holder of this work and the author uses the Dutch legislation to make this work public.



# Chapter 15

## Flight Path Planning in a Turbulent Wind Environment

Uwe Fechner and Roland Schmehl

**Abstract** To achieve a high conversion efficiency and at the same time robust control of a pumping kite power system it is crucial to optimize the three-dimensional flight path of the tethered wing. This chapter extends a dynamic system model to account for a realistic, turbulent wind environment and adds a flight path planner using a sequence of attractor points and turn actions. Path coordinates are calculated with explicit geometric formulas. To optimize the power output the path is adapted to the average wind speed and the vertical wind profile, using a small set of parameters. The planner employs a finite state machine with switch conditions that are highly robust towards sensor errors. The results indicate, that the decline of the average power output of pumping kite power systems at high wind speeds can be mitigated. In addition it is shown, that reeling out towards the zenith after flying figure eight flight maneuvers significantly reduces the traction forces during reel-in and thus increases the total efficiency.

### 15.1 Introduction

Converting the traction power of kites into electricity is a potential low cost wind energy solution. A minimal implementation is the pumping kite power system which harvests wind energy in a cyclic pattern, alternating between traction and retraction phases. During the traction phase the kite is flown in crosswind flight maneuvers which generates a high traction force that is used to drive a generator. During the retraction phase the kite is depowered and the generator is used as a motor to pull the kite back towards the ground station. The net energy output per cycle essentially

---

Uwe Fechner (✉) · Roland Schmehl  
Delft University of Technology, Faculty of Aerospace Engineering, Kluyverweg 1, 2629 HS Delft,  
The Netherlands  
e-mail: [fechner@aenarete.eu](mailto:fechner@aenarete.eu)

depends on the values of the traction force, reeling speed and time duration of both phases [5].

A key advantage of this energy harvesting technique is the possibility to adjust and modify these operational parameters and the three-dimensional flight path of the wing within a broad range. In practice the operational envelope is constrained by hardware limits of the wing, the tether and the control system, limits of the governing flight physics and safety limits. The purpose of the flight path planner is to design the operation for optimal performance while complying to the imposed constraints. It is an indispensable functional unit of a kite power system, translating the technical capabilities of the system and the characteristics of the deployment scenario into an optimal energy harvesting process.

Sophisticated methods for maximizing the energy output from a closed flight path, combining reel-in and reel-out within a single figure eight flight maneuver, have been described in literature [14]. With some restrictions these methods can also be applied for a flight path concatenating multiple circular maneuvers within a reel-out phase [15]. However, the described methods have two practical limitations. Firstly, only very simple system models can be used during the optimization process. This makes it impossible to realistically account for operational constraints in a turbulent wind field, such as, for example, the maximum tether force. This limiting force strongly depends on the tether sag which is generally neglected by fast, analytic system models. Secondly, the publications cited above do not include a crest factor of the power. This means that the power was optimized without accounting for important operational limits such as maximum power or force. As consequence the trajectories are of limited practical relevance.

In [29, 30] the optimal average position of the kite in the wind window is determined, i.e. the average azimuth and elevation angles which maximize the energy output. The proposed algorithm to find the average wind direction is effective and can in principle be combined with the flight path planner described in the present chapter. Not investigated in the cited publications is how to limit the power at high wind speeds and how a realistic wind profile affects the optimal average elevation angle.

In [27, 28] the control of the kite during retraction is investigated, proposing a flight path at the side of the wind window at an azimuth angle of  $45^\circ$ . The authors do not provide any evidence that this is the optimal path to reel in the kite. The focus of the cited publications is the control of the retraction phase and not the planning of the flight path. Furthermore, the required transitioning from retraction to traction and the impact on the power production is not investigated.

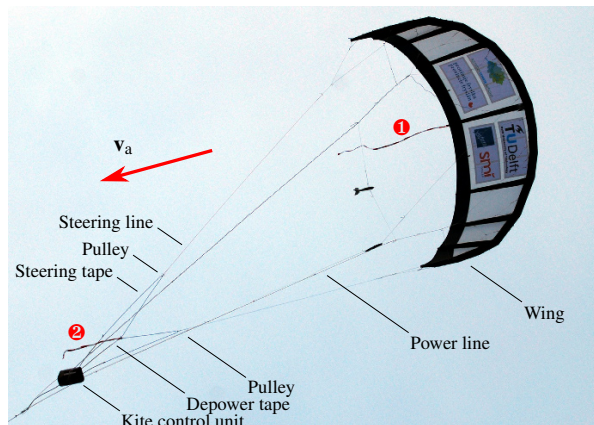
The focus of [21] is the control and flight performance of a tethered rigid wing system. The flight path planning is based on a lemniscate curve which is discretized by a large number of attractor points. As consequence, a large number of control commands have to be executed per flight maneuver and control loop delays can accordingly be more problematic. During retraction the aircraft pitches down and flies a waypoint track directed towards the ground station, while during traction a constant elevation angle is used. These design decisions are partially related to the rigid wing designed used in the study.

The chapter is organized as follows. In Sect. 15.2 we analyze the kinematics of tethered flight and the mechanism of steering, introduce a suitable kinematic model for path planning and improve the modeling quality of the wind resource by accounting for a realistic vertical profile and turbulence characteristics of the wind velocity. In Sect. 15.3 we present a planning approach for constructing the flight path from straight line and circle segments defined in terms of spherical surface coordinates. The approach can be used for both the retraction and traction phases providing a smooth transition and it can be optimized using a small set of parameters. The crest factors for traction force and power were carefully optimized to harvest the maximum average power for a given hardware without compromising the robustness. In Sect. 15.4 the performance of the flight path planner is assessed by simulating pumping cycle operation using a dynamic system model in conjunction with a wind turbulence model. Some of the design objectives are verified by a subsequent quasi-steady analysis. The preliminary content of the present chapter has been presented at the Airborne Wind Energy Conference 2015 [13] and is also published in [11].

## 15.2 Tethered Flight in a Realistic Wind Environment

The control strategy for the kite power system is closely connected to the available flight and winch control mechanisms, the resulting mathematical description of the control problem and the effect on the kinematics and dynamics of the system. The practical control approach presented in the following is based on the 20 kW demonstrator system designed, built and tested by Delft University of Technology [9, 18, 22, 26]. The flying components of this system are illustrated in Fig. 15.1.

**Fig. 15.1** Kite system consisting of a flexible membrane wing with 25 m<sup>2</sup> total surface area, a bridle line system to transfer the aerodynamic load and a suspended, remote-controlled cable robot (kite control unit) [18]. For this specific flight a piece of barricade tape ① is attached to the rear end of the center strut of the kite and another piece ② is attached to the end of the depower tape to indicate the direction of the apparent wind (24 November 2010)



### 15.2.1 Reference Frames and Kinematics of Tethered Flight

To describe the flight of a tethered wing in a wind field we define the wind reference frame  $x_w, y_w, z_w$  as illustrated in Fig. 15.2. The origin  $O$  of this Cartesian reference

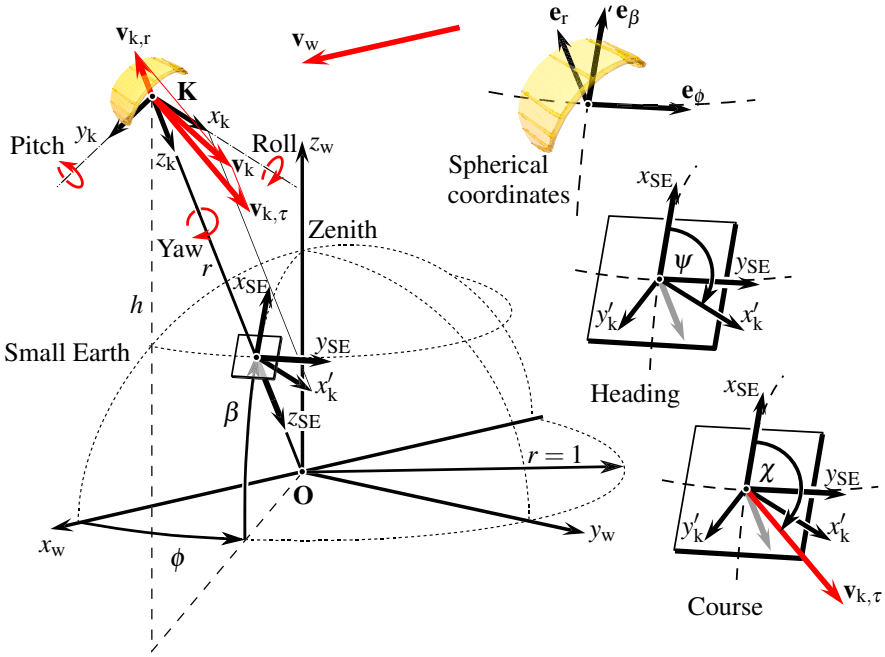


**Fig. 15.2** Wind reference frame  $x_w, y_w, z_w$ , small earth reference frame  $x_{SE}, y_{SE}, z_{SE}$ , kite reference frame  $x_k, y_k, z_k$ , spherical coordinates  $(r, \phi, \beta)$  and corresponding local vector base  $e_r, e_\phi, e_\beta$  to describe the flight of a tethered wing in a wind field. The course angle  $\chi$  describes the orientation of the tangential velocity of the kite with respect to the local  $x_{SE}$ -axis. Depicted is the ideal case of a straight tether for which the  $z_k$ - and  $z_{SE}$ -axes are aligned and the heading angle  $\psi$ , also denoted as yaw angle, describes the orientation of the kite with respect to the local  $x_{SE}$ -axis

frame is located at the ground attachment point of the tether and the  $x_w$ -axis is pointing in the direction of the average wind velocity  $v_w$ . We introduce spherical coordinates  $(r, \phi, \beta)$  to decompose the translational motion of the wing into radial and tangential components

$$\mathbf{v}_k = r\dot{\mathbf{e}}_r + r\dot{\phi} \cos \beta \mathbf{e}_\phi + r\dot{\beta} \mathbf{e}_\beta, \tag{15.1}$$

$$= \mathbf{v}_{k,r} + \mathbf{v}_{k,\tau}, \tag{15.2}$$

from which the following kinematic relations can be derived

$$v_{k,r} = \dot{r}, \quad (15.3)$$

$$v_{k,\tau} = r\sqrt{\dot{\phi}^2 \cos^2 \beta + \dot{\beta}^2}. \quad (15.4)$$

Defining the angular velocity of point  $\mathbf{K}$  with respect to origin  $\mathbf{O}$  as

$$\omega = \sqrt{\dot{\beta}^2 + \dot{\phi}^2 \cos^2 \beta}, \quad (15.5)$$

Eq. (15.4) can be reformulated as

$$v_{k,\tau} = r\omega. \quad (15.6)$$

The radial and tangential motion components are governed by two different control systems. Assuming that the tether is always tensioned, the radial velocity  $v_{k,r}$  is determined by the winch controller of the ground station. The direction of the tangential velocity vector  $\mathbf{v}_{k,\tau}$  is described by the course angle  $\chi$  and controlled by the steering system of the wing. The velocity magnitude  $v_{k,\tau}$ , however, is depending on the angle between tether and wind velocity vector, the reeling velocity of the tether, the aerodynamic properties and the mass of the wing [23].

The geometric similarity of tethered flight at constant radial distance and level flight of an aircraft above the curved surface of the earth motivates the use of a small earth analogy [17, 18]. The corresponding small earth coordinate system is defined on the surface of the unit sphere around the ground attachment point of the tether, using longitude  $\phi$  and latitude  $\beta$  to describe the angular position of the kite. Following common practice in aerospace engineering, the local reference frame  $x_{SE}, y_{SE}, z_{SE}$  is defined as a North, East, Down (NED) frame<sup>1</sup> with the local  $x_{SE}$ -axis pointing towards the zenith, the local  $y_{SE}$ -axis pointing towards East and the local  $z_{SE}$ -axis always pointing towards the origin  $\mathbf{O}$ .

The body-fixed reference frame of the kite has its origin at point  $\mathbf{K}$  and is denoted as  $x_k, y_k, z_k$  with unit vectors  $\mathbf{e}_{k,x}, \mathbf{e}_{k,y}, \mathbf{e}_{k,z}$ . As kite we define the entire flying system consisting of wing, bridle line system and suspended control unit [22, 26]. Following aerospace engineering practice, the  $y_k$ -axis defines the direction from the left to the right wing tip and the  $z_k$ -axis defines the direction from the wing to the suspended control unit, chosen such that the  $z_k$ -axis is aligned with the tether at the kite attachment point. The  $x_k$ -axis is by definition orthogonal to  $y_k$  and  $z_k$ . If the tether is not straight the  $z_k$ - and  $z_{SE}$ -axes are not aligned.

The rotations around the body-fixed  $x_k$ -,  $y_k$ - and  $z_k$ -axes are denoted as roll, pitch and yaw. For the ideal case of a fully tensioned, straight tether the pitch and roll rates, are kinematically coupled to the angular velocity  $\omega$  of point  $\mathbf{K}$ , as defined by Eq. (15.5). This specific situation, in which the yaw angle describes the heading of the kite on the unit sphere, is illustrated in Fig. 15.1. For a flexible and thus sagging tether the pitch and roll rotations are not kinematically coupled to the tangential flight motion of the kite.

<sup>1</sup> North, East, Down and zenith refer in this context to the small earth

## 15.2.2 Kinematic Kite Model and Steering Mechanism

For designing the flight path planner we will use an idealized kinematic model based on a straight tether as discussed in the previous section. The first three degrees of freedom of this model are the spherical coordinates  $(r, \phi, \beta)$  of the kite point  $\mathbf{K}$ . Because of the bridling of the wing, the pitch and roll rotations of the kite are kinematically coupled to the tangential motion of the kite, while the heading angle  $\psi$  is a fourth degree of freedom describing the rotation of the kite around the tether.

It is important to note that this kinematic model describes the translation and rotation of the entire kite system consisting of wing, bridle line system and suspended kite control unit. Within this system, the kite control unit actuates the bridle line system to deform and rotate the wing relative to the kite reference frame. The changing aerodynamic forces and moments induce accelerations that adjust the flight motion of the kite. From this perspective, the entire wing functions as an aerodynamic control surface similar to the control surfaces of an aircraft.

To avoid the physical modeling of the complex aeroelastic phenomena which govern the mechanism of steering [3, 4] we use an empirical correlation between the turn rate  $\dot{\psi}$  and the steering actuation of the bridle line system. This turn rate law has been established on the basis of experimental data [6–8, 18] and validated by numerical simulations [3]. As a result, the rotation of the kite around the tether is directly coupled to the prescribed control input.

The course angle  $\chi$  describes the direction of the tangential velocity  $\mathbf{v}_{k,\tau}$ . For the ideal hypothetical case of a massless kite ( $m = 0$ ) in a stagnant wind field ( $\mathbf{v}_w = 0$ ), the heading vector  $\mathbf{e}_{k,x}$  and the tangential velocity vector  $\mathbf{v}_{k,\tau}$  are aligned at all times which means that heading and the course angle are identical. This because kites and aircraft in general are designed to align with the relative flow velocity  $\mathbf{v}_a$ , when the flight condition does not require to compensate a lateral inertial or gravitational force component. For a stagnant wind field  $\mathbf{v}_a$  is parallel to the flight velocity  $\mathbf{v}_k$ . Any deviation from this ideal case leads to a misalignment of heading and course, which is quantified by the kinematic side slip angle [18].

For example, a non-vanishing wind velocity  $\mathbf{v}_w$ , which is a prerequisite for wind energy conversion, will incline the relative flow velocity with respect to the flight velocity according to the definition

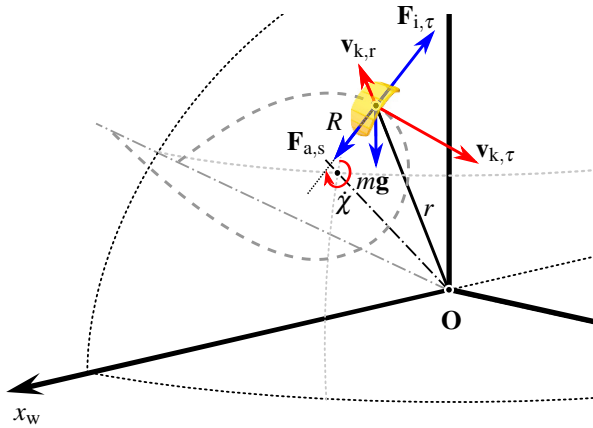
$$\mathbf{v}_a = \mathbf{v}_w - \mathbf{v}_k. \quad (15.7)$$

However, kites with a lift-to-drag ratio  $L/D \gg 1$  operate at crosswind flight speeds  $v_{k,\tau} \gg v_w$  and it is thus reasonable to neglect the misalignment of  $\mathbf{v}_a$  and  $\mathbf{v}_k$  in the traction phase.

For a real kite ( $m > 0$ ) inertial and gravitational force effects transverse to the tether have to be balanced by an aerodynamic side force  $\mathbf{F}_{a,s}$ . Given the constrained pitch and roll rotations this side force can only be generated by inclining the heading of the kite with respect to its course, thus enforcing a kinematic side slip angle. This mechanism is illustrated in Fig. 15.3 for a kite flying a left turn (perspective from ground) and including the effects of the gravitational force  $mg$  and centrifugal force



**Fig. 15.3** Kite performing a left turn ( $\dot{\chi} > 0$ ) while flying a downloop figure eight maneuver and generating traction power ( $v_{k,r} > 0$ ). Only one half of the maneuver is displayed. The dash-dotted line passing through the center of the turn is the turning axis, while the corresponding turn radius is denoted as  $R$  and the non-dimensional turning radius is defined as  $\varrho = R/r$



due the turning maneuver,

$$F_{i,\tau} = m \frac{v_{k,\tau}^2}{R}, \tag{15.8}$$

where the radius of curvature  $R$  characterizes the tangential motion component.

In the described kinematic framework, the turning radius  $R$  links the rate of change of the course angle  $\dot{\chi}$  to the tangential kite velocity  $v_{k,\tau}$  and, using Eq. (15.6), to the angular velocity  $\omega$  of the kite point

$$\dot{\chi} = \frac{v_{k,\tau}}{R} = \frac{r}{R} \omega = \frac{\omega}{\varrho}. \tag{15.9}$$

The relation between the heading of the kite and the relative flow is illustrated in Fig. 15.4 for three typical flight modes during pumping cycle operation. The flow direction is indicated by two pieces of red/white striped barricade tape, as described in the caption of Fig. 15.1. The end point of the depower tape, to which the two



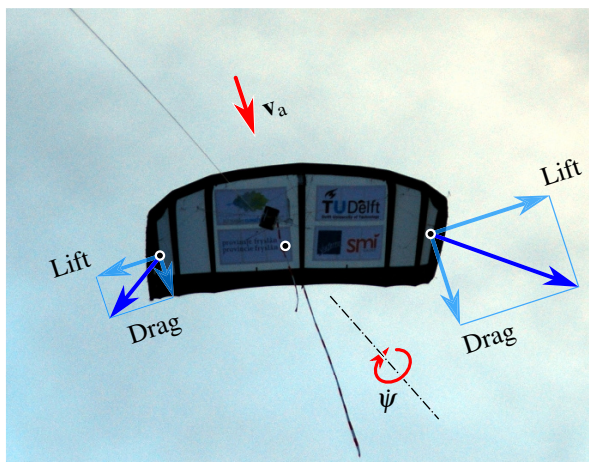
**Fig. 15.4** Wing and bridle line system during a downloop figure eight maneuver performing a right turn (left) and following straight flight diagonally upwards (center) and during retraction of the kite (right). Video stills taken from the kite control unit (24 November 2010)

steering tapes and the barricade tape in the foreground are tied, is highlighted by a dot. The barricade tape attached to the kite is indicated by an arrow.

When in crosswind flight (left & center) the wing is powered by reeling in the depower tape. This tensions the steering lines and consequently the highlighted knot stays in the line of sight from control unit to wing. When retracting the kite towards the ground station (right) the wing is depowered by reeling out the depower tape. This relaxes the steering lines which are deflected substantially by the relative flow.

To fly the turn, the kite needs to balance a centrifugal acceleration of 2 to 4g by generating an aerodynamic side force towards the turning axis. The strength of this force is indicated by the pronounced sideslip angle (the angle between center strut and attached barricade tape) in the left photo. The steering mechanism is illustrated in more detail in Fig. 15.5 including the generated aerodynamic steering forces acting on the wing tips. The sketch shows how the asymmetric steering input of reeling

**Fig. 15.5** Aerodynamic steering forces acting on a kite flying a right turn (perspective from ground). The forces at the wing tips are decomposed into lift and drag components. The dash-dotted line is in extension of the tether and indicates the yaw rotation axis. The center point indicated the approximate location around which the aerodynamic moment of the wing tips act. Photo of the kite, which has a total wing surface area of 25 m<sup>2</sup>, is taken from the ground (24 November 2010)



in the right and reeling out the left steering tape warps the entire wing, which leads to a resultant side force to the right which is required for the right turn. The importance of actively controlled wing warping for the excellent turning characteristics of C-shaped flexible membrane wings has been confirmed by computational analysis [4].

Because the kite control unit represents almost 50% of the total airborne mass it experiences a strong centrifugal force during the turns of the figure eight maneuvers. As can be seen in Fig. 15.4 (left) this leads to a substantial outwards deflection of the unit which distorts not only the entire bridle line system but also affects the video recording from this point of observation.

When flying diagonally upwards the kite needs to balance only the gravitational acceleration  $g$ . This is indicated by the comparatively small sideslip angle in the center photo. During retraction the kite asymptotically approaches a steady flight state which is characterized by a descent at constant elevation angle. As consequence, the

tangential velocity  $v_{k,\tau}$  and angular velocity  $\omega$  can become very small towards the end of the retraction phase. In this situation of undefined course angle, the heading of the kite is planned to keep the nose of the kite pointing towards zenith.

To summarize the above considerations we conclude that an asymmetric steering input leads to an aerodynamic side force. Instead of using a dynamic model we couple the turn rate  $\dot{\psi}$  of the kite directly to the steering input by using an empirical turn rate law. On the other hand, the rate of change of the course angle  $\dot{\chi}$  is governed by the tangential flight velocity  $v_{k,\tau}$  of the kite, which is a dependent variable, and by the turn radius  $R$  required for a specific maneuver.

The objective of the steering system is to control the course angle to fly the kite towards any feasible attractor point or on a turn with well-defined radius. This is achieved by controlling the steering signal to the kite control unit. By introducing the small earth analogy and using the course angle as the controlled variable the kite control problem is reduced to a Single Input Single Output (SISO) problem [2].

### 15.2.3 Wind Resource

Within the scope of this study we limit the pumping cycle operation to a maximum altitude of 600m and a minimum tether length of 300m. We further assume that the maximum altitude and maximum tether length are identical, although a safety margin will have to be applied for any practical use of the results. To cover the operational altitude range we use wind data measured with the 213m high KNMI-mast in Cabauw, The Netherlands, in 2011. The publicly available CESAR database provides data for different altitudes, sampled with 10min resolution for at least a full year [24].

The average ground wind speed, measured at a height of 10m, is 4.26m/s. The corresponding estimated cumulative probability distribution function (CDF) is shown in Fig. 15.6. The performance simulations are based on a kite power system which is designed to reach its nominal power at a wind speed that is exceeded about 20% of the time. According to the CDF this threshold is at a ground wind speed of 6m/s. For this choice a capacity factor of about 40% is expected.

The measured vertical profile of the average wind speed is shown in Fig. 15.7. The diagram includes the fitted power law [1]

$$v_w = v_{w,g} \left( \frac{\bar{z}}{z_{\text{ref}}} \right)^\alpha, \quad (15.10)$$

with the ground wind speed  $v_{w,g}$  at  $z_{\text{ref}} = 10$  m height, and the average height  $\bar{z}$  of the kite during the traction phase. Average wind speeds of 7.28 and 8.56m/s at 98.7 and 131.6m altitude were estimated. These heights correspond to the average operational altitude of the kite during the traction phase, as will be shown in Sect. 15.4.

Wind turbulence is characterized by the relative intensity  $I$  of the turbulent velocity fluctuations. To account for the sampling interval of the experimental data,

**Fig. 15.6** Cumulative probability distribution function (CDF) of the ground wind speed at Cabauw, The Netherlands, in 2011. Data from [24]

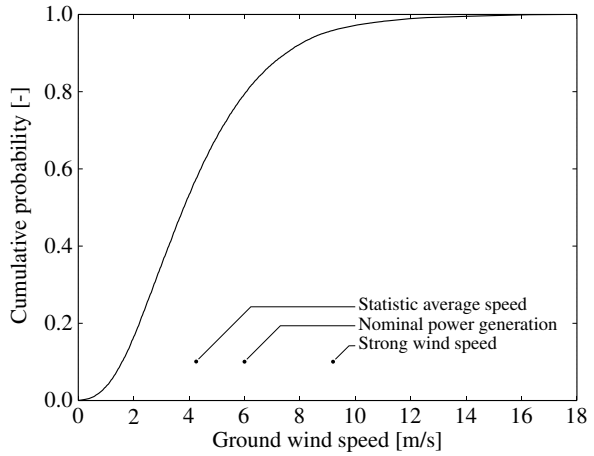
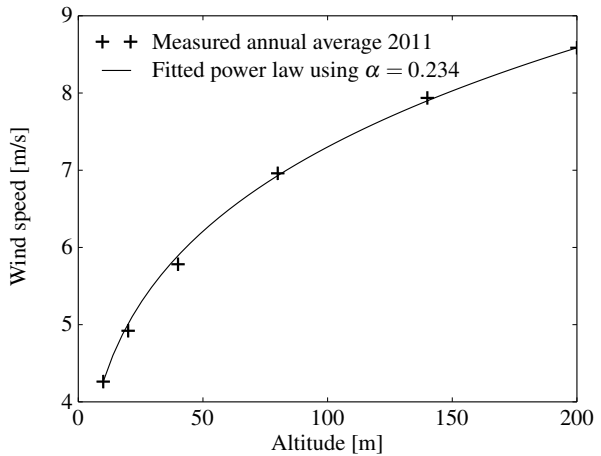


**Fig. 15.7** Vertical profile of the wind speed measured at Cabauw in 2011 [24] and fitted power law with an exponent  $\alpha = 0.234$



we define this intensity as the ratio of the standard deviation  $\sigma_1$  of the wind speed within 10min intervals and the corresponding 10min average of the wind speed. Three-dimensional turbulence is simulated using the approach described in [19, 20] for the three different ground wind speeds displayed in Fig. 15.6 and listed in Table 15.1.

**Table 15.1** Simulation scenarios based on Cabauw data [24].  $I_{99}$  and  $I_{197}$  are intensities at 98.7 m and 197.4 m

Ground wind speed	$v_{w,g}$	$I_{99}$	$I_{197}$
Annual average	4.26 m/s	8.5%	6.3%
Nominal power generation	6.00 m/s	9.7%	7.2%
Reel-out depower required	9.20 m/s	9.8%	7.9%

Parameter	Value	Description
$\gamma$	3.9	anisotropy parameter, isotropic turbulence $\gamma = 0$
$\sigma_1$	see Table 15.1	standard deviation of the wind component at the average height during reel-out in the mean wind direction
$\sigma_{iso}$	$0.55 \sigma_1$	standard deviation of wind speed for isotropic turbulence
$l$	33.6 m	turbulence length scale for an average height $> 60$ m

**Table 15.2** Parameters of the Mann model used to generate the three-dimensional wind field, from IEC 61400 [16]

The homogeneous velocity field is obtained by three-dimensional Fast Fourier Transformation (FFT) of the spectral tensor. A white noise vector is used to give the wave numbers a random phase and amplitude. The model parameters are listed and described in Table 15.2. The ground wind speed of 9.20 m/s marks the upper limit of pumping cycle operation without the need to depower the wing during tether reel-out in the traction phase.

For each value of the ground wind speed, a turbulent wind field is computed on a grid of  $4050 \times 100 \times 500$  nodes, using a uniform spatial resolution of 2 m. The size of the computational domain in  $x$ -direction is large enough to cover 10 min of kite operation with uniquely simulated wind data, as illustrated in Fig. 15.8.

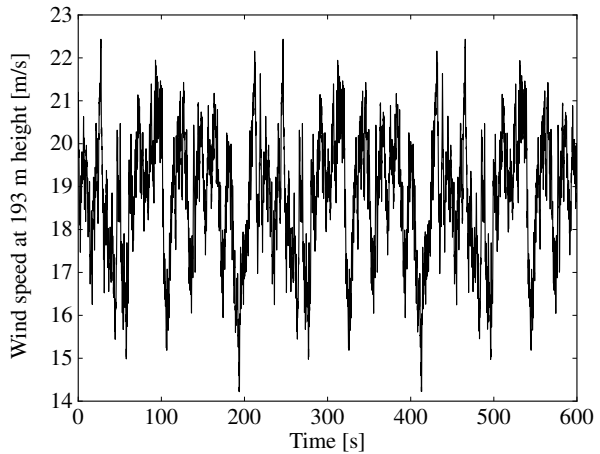


**Fig. 15.8** Simulated wind speed as function of time for the scenario  $v_{w,g} = 9.2$  m/s. The wind speed varies between 14.2 and 22.5 m/s and changes can be as fast as  $4 \text{ m/s}^2$

It should be noted that the kite is substantially larger than the spatial discretization of the wind field. We thus use a third-order spline interpolation to determine the three-dimensional wind velocity vector at any given position in the computational domain. The time dependency of the wind is taken into account by an advection correction, adding the product of simulation time and average wind speed at the height of the kite to its  $x$ -position before determining the wind velocity vector by interpolation of pre-computed grid data.

## 15.3 Flight Path Planner

The objective of the planning algorithm is to provide an optimal flight path as a function of the variable wind conditions and the various operational constraints of the system. If multiple systems are arranged in a wind park configuration, as analyzed in Chap. 16, additional constraints due to joint operation have to be considered.

### 15.3.1 General Design Considerations

Path planning can be based on an ordered list of positions, so-called waypoints, that describe the path to be tracked by the kite. Alternatively, the desired path can also be described as a continuous curve [2, 17, 18]. It is the task of the flight control algorithm to generate steering commands that maneuver the kite from any deviating position back to this reference path. A variant is to steer the kite sequentially towards attractor points without the goal to actually reach and pass these points. For example, the original flight path planner of the 20 kW demonstrator of Delft University of Technology uses four attractor points to describe a complete figure eight flight maneuver [26], while the path planner developed by Ampyx Power uses a substantially larger number of attractor points to describe this maneuver [21].

In the present study we adopt this alternative approach, however, instead of using attractor points only, we introduce additional turning maneuvers, with well-defined center point and radius, to advance from one attractor point to the next. This planning scheme is illustrated schematically in Fig. 15.9, combining two attractor points  $P_3$  and  $P_4$  with two turns around points  $C_2$  and  $C_3$  to describe the figure eight maneuvers. An important design constraint is the minimum turning radius  $R_{\min}$  of the kite which is not only determined by the inherent maneuverability of the wing, but also by the operational limits of integrated sensors. One example are the GNSS sensors which tend to fail when the turning radius is too small.

It is important to note that the depicted representation by linear and circular segments in the  $\phi\beta$ -plane is only a geometric approximation of the planned flight path. This true path is constructed in three-dimensional Cartesian space according to basic flight-physical considerations. For example, we assume that for straight flight at constant tether length the kite moves along a great circle. Also denoted as a geodesic, this circular arc segment represents the shortest distance between two positions on the spherical surface. Similarly we assume that for a turn with constant radius and at constant tether length the kite moves along a small circle. Both type of arc segments can be used to construct a figure eight flight maneuver.

However, because the angular coordinates  $\phi$  and  $\beta$  describe a spherical coordinate surface in Cartesian space, the mapping of these segments to the  $\phi\beta$ -plane introduces a geometric distortion. This distortion increases with the elevation angle and reaches a maximum at the zenith. For the purpose of simplicity and because the planned path is not explicitly tracked we neglect this effect in Fig. 15.9 using straight lines and circle segments to illustrate the flight path.

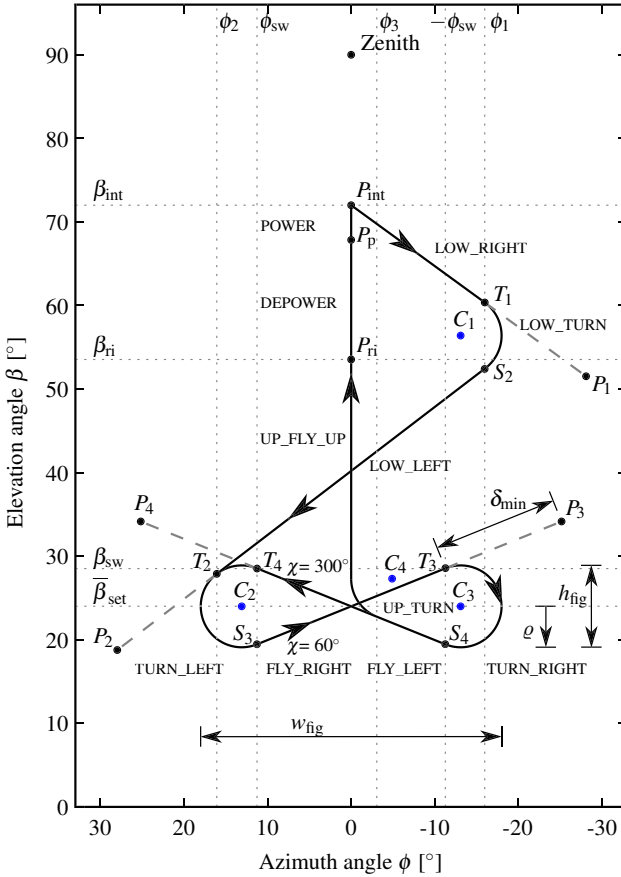


**Fig. 15.9** Planned pumping cycle with downloop figure eight maneuvers at an average elevation angle of  $\bar{\beta}_{set} = 24^\circ$ , represented in the  $\phi\beta$ -plane. The entire cycle is described by five attractor points ( $P_1$  to  $P_4$  and zenith) and four turning points ( $C_1$  to  $C_4$ ). The minimum angular distance between kite and an active attractor point is  $\delta_{min} = 15^\circ$ . This threshold value for  $\delta$  is used to trigger the turning maneuvers. Adapted from [11, 12]

Following the crosswind operation, the kite performs a turn around point  $C_4$  into the  $x_w z_w$ -plane to fly towards zenith. When reaching the elevation angle  $\beta_{ri}$  the kite is depowered by reeling out the depower tape. As consequence, the tether force drops and the retraction phase can begin. When the minimum tether length is reached at  $P_p$  the depower tape is reeled in to power the kite again. When the target power setting is reached the transition phase begins in which the kite is steered towards  $P_1$ . The position of  $P_p$  is not planned by the algorithm, but measured and used as input for the planned flight path. In the first cycle  $P_p$  is identical to the parking position.

Reeling in while steering towards zenith has the advantages that for one, the wind speed in the direction of the tether and thus the retraction force is low. For the other, the kite is rising at the end of the traction phase, increasing its potential energy, which later helps to power the retraction phase. The use of potential energy is more efficient than using electrical storage only. If the traction energy is converted into electricity, stored in a battery and then a portion of it is used to drive a motor to retract the kite, this has an efficiency of about  $\eta = 90\% \cdot 80\% \cdot 95\% = 68.4\%$ . The three contributions are the estimated generator, motor and battery efficiencies. Potential energy can be used without any losses to reduce the tether forces during retraction. Within certain limits a heavier kite thus increases the overall efficiency. On the other hand a higher mass of the kite makes launching and landing more difficult and increases the minimum wind speed required for operation.

Flying towards an intermediate point after the retraction phase helps to mitigate the tether force peak which can otherwise occur when the kite is diving too rapidly towards the ground. We concluded that a combination of flying towards attractor points and turn actions allows planning of an any technically feasible flight path. Our tests have show that when limiting the duration of the turn actions in time the flight control is very robust against sensor or communication failures.

To conclude the above considerations we summarize the following goals for the design of the flight path planner:

1. a high projected wind speed  $\mathbf{v}_w \cdot \mathbf{e}_r$  at the height of the kite in the traction phase;
2. a low crest factor (ratio of peak value to effective value) of the reel-out force and reel-out power;
3. a large turn radius  $R$  to limit the steering effort and the additional aerodynamic drag caused by steering;
4. a low steering effort also when flying straight;
5. a retraction phase with low projected wind speed;
6. short transition phases between retraction and traction;
7. low tether force overshoot at the transition from retraction to traction;
8. high robustness with respect to sensor errors and delays;
9. good controllability of the maximum and minimum height;
10. good controllability of the projected wind speed and thus reel-out power, especially at high wind speeds, but also at medium wind speeds with high turbulence.

The design goals (2) and (3) are competing, as do the goals (6) and (7), and a good design accordingly requires a compromise solution.

### ***15.3.2 Supervisory Control for Automated Power Production***

The proposed supervisory control for operation in pumping cycles is shown in Fig. 15.10. The path is planned in the two-dimensional plane spanned by the azimuth and elevation angles. The initial condition for automated power production is



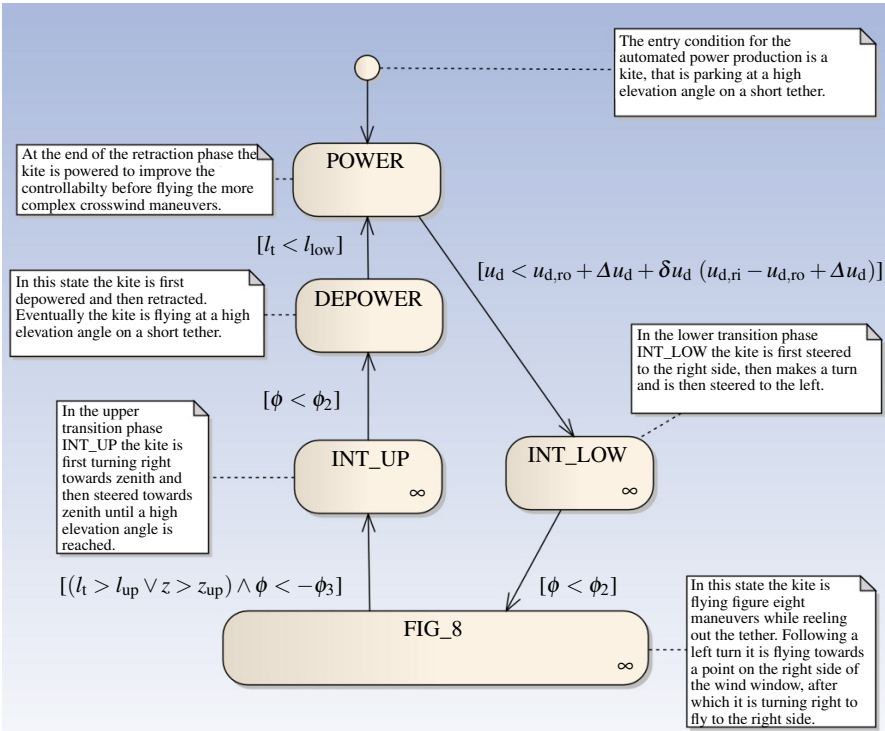


**Fig. 15.10** Finite state diagram detailing the supervisory controller for automatic operation in pumping cycles. To start the traction phase the minimum tether force for the winch controller is reduced to about 10% of the maximum tether force. This results in an attenuation of the reel-out speed and a reversal of the drum rotation from reel in to reel out, because the winch controller now tracks a set speed, that is positive and proportional to the square-root of the force. Adapted from [11]

a parking position of the kite at a high elevation angle on a short tether ( $l_t = l_{low}$ ). When activated, the supervisory controller enters the state POWER. In this state, the angle of attack of the wing is increased to the set value for tether reel out. When this target is reached to at least  $\delta u_d$  percent the controller is switching into the lower transition phase INT\_LOW. In this state the kite is first flying to the right, then makes a turn and is finally flying to point  $P_2$  on the left of the wind window. When an azimuth angle  $\phi > \phi_2$  on the figure eight trajectory is reached the kite enters the state FIG\_8.

In this state the kite is forced to fly figure eight maneuvers, the tether is reeled out and power is harvested. When either the height of the kite or the tether length reach an upper limit and the kite is near the center of the wind window, then the controller switches into the upper transition state INT\_UP.

The upper transition phase begins with a turn towards zenith. Then the kite is flying straight upwards, slowing down while the kite is still harvesting energy. When the wind speed dependent elevation angle  $\beta_{ri}$  is reached the controller switches into

State	Next state	$u_{d,set}$	Condition
PARKING	POWER	$u_{d,ro} + \Delta u_d$	Event START_POWER_PRODUCTION
POWER	INT_LOW	$u_{d,ro} + \Delta u_d$	$u_d < u_{d,ro} + \Delta u_d + \delta u_d (u_{d,ri} - u_{d,ro} - \Delta u_d)$
INT_LOW	FIG_8	$u_{d,ro} + \Delta u_d$	Event EXIT(INT_LOW)
FIG_8	INT_UP	$u_{d,ro} + \Delta u_d$	Event EXIT(FIG_8)
INT_UP	DEPOWER	$u_{d,ro} + \Delta u_d$	Event EXIT(INT_UP)
DEPOWER	POWER	$u_{d,ri}$	$l_t < l_{low}$

**Table 15.3** Finite states and state transitions of the supervisory flight path controller during automated power production. This controller activates one of the sub-controllers for the planning of the flight sections. In addition it changes the angle of attack of the kite by changing the depower setting  $u_d$

the state DEPOWER. In this state the angle of attack of the wing is reduced for depowering and the set value of the tether force is reduced. After a short transition time the winch begins to reel in.

In the state DEPOWER the elevation angle increases. When the lower tether length is reached ( $l_t = l_{low}$ ) the controller switches to the lower transition state INT\_LOW and the next pumping cycle begins.

The state transition table for the supervisory control is shown in Table 15.3. The settings of the winch depend on the state of the supervisory flight path controller. The value  $\Delta u_d$  is calculated by the winch controller. It is an additional depowering of the kite for limiting the power output at high wind speeds.  $\delta u_d$  is a constant in the order of 70% and determines to which degree the powering has to be finished before flying to the side.

### 15.3.3 Lower Transition Phase

The design of the lower transition phase aims at the following objectives:

- a low tether force overshoot. This overshoot is caused by the gravitational acceleration of the kite flying downwards,
- a minimum impact on total efficiency. If the kite is flying too far to the side of the wind window to limit the force overshoot, too much time and energy is lost,
- a low undershoot of the minimum elevation angle. This prevents that the kite flies too close to the ground, which is a safety risk, and also reduces the power output because of the lower wind velocities towards the ground.

The proposed layout of the flight path is illustrated schematically in Fig. 15.9 by the segments LOW\_RIGHT, LOW\_TURN and LOW\_LEFT. The implementation keeps the rate of change of the elevation angle identical to the value during the straight flight segments of the figure eight maneuvers. The state transition table is shown in Table 15.4. Because the path construction depends on the desired change rate of  $\beta$ , we explain the calculation of  $\phi_1$  at the end of the next section.

State	Next state	$\mathbf{p}_{k,\text{set}}^{\text{SE}}$	$\dot{\chi}_{\text{set}}$	Condition
Initial	LOW_RIGHT	$P_1$	from PID	always
LOW_RIGHT	LOW_TURN	—	$\dot{\chi}_{\text{turn}}$	$\phi < \phi_1$
LOW_TURN	LOW_LEFT	$P_2$	from PID	$\chi < 180 + \delta\chi_{\text{int}}$
LOW_LEFT	Final	—	$-\dot{\chi}_{\text{turn}}$	$\phi > \phi_2$

**Table 15.4** Finite sub-states of the lower transition phase INT\_LOW. The parameter  $\delta\chi_{\text{int}}$  is introduced to compensate the delay of the steering actuator and the inertia of the kite at the end of the turn. It is chosen such that the kite does not turn more than required before flying straight towards the attractor point  $P_2$

### 15.3.4 Traction Phase and Crosswind Flight Maneuvers

The four-step flight path planner for flying figure eight maneuvers during the traction phase is shown in Fig. 15.9. Flying past point  $T_2$  the kite first turns left, then steers towards  $P_3$ , then turns right and finally steers towards  $P_4$ , after which the sequence is repeated. Table 15.5 describes the outputs and the switch conditions of the six different sub-states for flying figure eight maneuvers.

State	Next state	$\mathbf{p}_{k,\text{set}}^{\text{SE}}$	$\dot{\chi}_{\text{set}}$	Condition
Initial	TURN_LEFT	—	$\dot{\chi}_{\text{turn}}$	always
FLY_LEFT	TURN_LEFT	—	$\dot{\chi}_{\text{turn}}$	$\phi > \phi_{\text{sw}}$
TURN_LEFT	FLY_RIGHT	$P_3$	from PID	$\chi > 270^\circ - \delta\chi$
FLY_RIGHT	TURN_RIGHT	—	$-\dot{\chi}_{\text{turn}}$	$\phi < -\phi_{\text{sw}}$
TURN_RIGHT	FLY_LEFT	$P_4$	from PID	$\chi < 90^\circ + \delta\chi$
FLY_LEFT	LAST_LEFT	—	from PID	$(l_t > l_{\text{up}} \vee z > z_{\text{up}}) \wedge \phi \leq \phi_3$
LAST_LEFT	Final	—	$-\dot{\chi}_{\text{turn}}$	$\phi > \phi_3$
FLY_RIGHT	LAST_RIGHT	—	from PID	$(l_t > l_{\text{up}} \vee z > z_{\text{up}}) \wedge \phi \geq -\phi_3$
LAST_RIGHT	Final	—	$\dot{\chi}_{\text{turn}}$	$\phi < -\phi_3$

**Table 15.5** Finite sub-states of the figure eight flight path planner. Flying these maneuvers is not finished before the upper height  $z_{\text{up}}$  or the upper tether length  $l_{\text{up}}$  is reached. The final up-turn is always started such that it ends at  $\phi = 0$ . The parameter  $\delta\chi$  is introduced to compensate the delay of the steering actuator and the inertia of the kite at the end of the turn. It is chosen such that the kite does not turn more than required before flying straight towards one of the attractor points

The path planner has the following inputs and outputs:

- IN: set value of the average elevation angle  $\bar{\beta}_{\text{set}}$ ,
- IN: course angle  $\chi$  and heading angle  $\psi$ ,
- IN: azimuth angle  $\phi$ ,
- OUT: boolean value  $PID_{\text{active}}$ ,
- OUT: set value of the position  $\mathbf{p}_{k,\text{set}}^{\text{SE}}$  when the PID is active.
- OUT: set value for the turn rate  $\dot{\psi}_{\text{set}}$  when the PID is not active.

The path is parametrized by the angular width  $w_{\text{fig}}$  and height  $h_{\text{fig}}$  of the figure eight and the minimum angular distance  $\delta_{\text{min}}$  between kite and an active attractor point. When the angular distance  $\delta$  from the currently active attractor point drops below this threshold value the next turning maneuver is triggered. When these values are given,  $P_3, P_4, \psi_{\text{turn}}$  and  $\phi_{\text{sw}}$  can be calculated.

As a first step we calculate the non-dimensional turning radius  $\varrho = h_{\text{fig}}/2$  as a linear function of the average elevation angle  $\bar{\beta}_{\text{set}}$

$$\varrho = \varrho_{\text{max}} - (\varrho_{\text{max}} - \varrho_{\text{min}}) \frac{\bar{\beta}_{\text{set}} - \beta_{\text{min}}}{\beta_{\text{max}} - \beta_{\text{min}}}, \quad (15.11)$$

using the constant values

$$\beta_{\text{min}} = 20^\circ, \quad \beta_{\text{max}} = 60^\circ, \quad \varrho_{\text{min}} = 3^\circ, \quad \varrho_{\text{max}} = 5^\circ, \quad (15.12)$$

that have been determined empirically for the 20 kW demonstrator system illustrated in Fig. 15.1. Equation (15.11) decreases the turning radius with increasing average elevation angle of the flight maneuvers. This suppresses the kinematically induced variation of the effective wind speed  $\mathbf{v}_w \cdot \mathbf{e}_r$  which, for constant turning radius, would increase towards the zenith. Using the measured angular velocity  $\omega$  of the kite the required turn rate  $\dot{\chi}_{\text{turn}}$  can then be calculated from Eq. (15.9).

In a next step, the azimuth angle of the turning point  $C_2$  is calculated as

$$\phi_{C2} = \frac{w_{\text{fig}}}{2} - \varrho \quad (15.13)$$

and the angular coordinates of the switch points  $T_3 = (-\phi_{\text{sw}}, \beta_{\text{sw}})$  and  $T_4 = (\phi_{\text{sw}}, \beta_{\text{sw}})$  are determined from the equations of the right turning circle and the tangent as

$$\phi_{\text{sw}} = \phi_{C2} - \frac{\varrho^2}{\phi_{C2}}, \quad \beta_{\text{sw}} = \bar{\beta}_{\text{set}} + \sqrt{\varrho^2 - (\phi_{\text{sw}} - \phi_{C2})^2}. \quad (15.14)$$

The slope  $k$  of the straight line from  $S_4$  via  $T_4$  to  $P_4$  can now be calculated as

$$k = \sqrt{\frac{\phi_{C2} - \phi_{\text{sw}}}{\phi_{\text{sw}}}} \quad (15.15)$$

and the angular coordinates of the attractor points  $P_3 = (-\phi_P, \beta_P)$  and  $P_4 = (\phi_P, \beta_P)$  are determined as

$$\phi_P = \phi_{\text{sw}} + \delta_{\text{min}} \sqrt{\frac{1}{1+k^2}}, \quad \beta_P = \beta_{\text{sw}} + \delta_{\text{min}} k \sqrt{\frac{1}{1+k^2}}. \quad (15.16)$$

We chose the azimuth angle of  $C_1$  to be equal to the azimuth angle of  $C_3$

$$\phi_{C1} = \phi_{C3} = -\phi_{C2}, \quad (15.17)$$

and accordingly calculate its elevation angle as

$$\beta_{C1} = \beta_{\text{int}} - k_1 + k_2 \bar{\beta}_{\text{set}}. \quad (15.18)$$

The coefficients  $k_1$  and  $k_2$  are determined empirically, such that

- for  $\bar{\beta}_{\text{set}} = \beta_{\text{max}}$  the turning points  $C_1$  and  $C_3$  coincide to avoid an overshoot of the tether force during the first pumping cycle and
- for  $\bar{\beta}_{\text{set}} = \beta_{\text{min}}$  the worst case tether force overshoot is negligible while the time for the lower transition phase is still as short as possible.

Within the scope of this chapter this is achieved by the following values

$$k_1 = 18.6^\circ, \quad k_2 = 0.11. \quad (15.19)$$

In a next step,  $\phi_1$  is calculated as

$$\begin{aligned} \phi_1 = & \frac{1}{\phi_{C1} (\beta_{C1}^2 - 2\beta_{C1}\beta_{\text{int}} + \beta_{\text{int}}^2 + \phi_{C1}^2)} \left( \beta_{C1}^2 \phi_{C1}^2 - 2\beta_{C1}\beta_{\text{int}}\phi_{C1}^2 \right. \\ & - \beta_{C1} \sqrt{\phi_{C1}^2 r^2 (\beta_{C1}^2 - 2\beta_{C1}\beta_{\text{int}} + \beta_{\text{int}}^2 + \phi_{C1}^2 - \varrho^2)} + \beta_{\text{int}}^2 \phi_{C1}^2 \\ & \left. + \beta_{\text{int}} \sqrt{\phi_{C1}^2 \varrho^2 (\beta_{C1}^2 - 2\beta_{C1}\beta_{\text{int}} + \beta_{\text{int}}^2 + \phi_{C1}^2 - r^2)} + \phi_{C1}^4 - \phi_{C1}^2 \varrho^2 \right). \end{aligned} \quad (15.20)$$

The elevation angle  $\beta_{\text{int}}$  at the beginning of the lower transition phase is measured. For the schematic shown in Fig. 15.9 we assume a value of  $\beta_{\text{int}} = 72^\circ$ . To determine  $\phi_2$  we use the geometric fact that the flight path during the state LOW\_LEFT must cross the line  $\phi = 0$  at the average elevation angle of the turning points  $C_1$  and  $C_2$

$$\beta_M = \frac{1}{2} (\beta_{C1} + \beta_{C2}). \quad (15.21)$$

With these parameters the azimuth angle  $\phi_2$  is calculated as

$$\begin{aligned} \phi_2 = & \frac{1}{\beta_M^2 - 2\beta_M\beta_{C1} + \beta_{C1}^2 + \phi_{C1}^2} \left( -\beta_M^2\beta_{C1} + 2\beta_M\beta_{C1}^2 - \beta_M \varrho^2 - \beta_{C1}^3 \right. \\ & \left. - \beta_{C1}\phi_{C1}^2 + \beta_{C1} \varrho^2 + \sqrt{\phi_{C1}^2 \varrho^2 (\beta_M^2 - 2\beta_M\beta_{C1} + \beta_{C1}^2 + \phi_{C1}^2 - \varrho^2)} \right). \end{aligned} \quad (15.22)$$

Using the basic rules of geometry the azimuth angle, needed in the exit condition of Table 15.5, is evaluated as

$$\phi_3 = \varrho - \sqrt{\frac{k^2 \varrho^2}{k^2 + 1}}. \quad (15.23)$$

### 15.3.5 Upper Transition Phase

The design of the upper transition phase aims at the following objectives:

- bringing the kite out of the power zone, while still harvesting energy,
- implementing a fast and smooth transition.

The state transition table of the upper transition phase is shown in Table 15.6. The optimal elevation angle  $\beta_{ri}$  at which the traction phase is terminated depends on the wind conditions. A first estimate can be calculated as

$$\beta_{ri} = k_5 + k_6 \bar{\beta}_{set} \quad (15.24)$$

with

$$k_5 = 37.5^\circ, \quad k_6 = 0.5. \quad (15.25)$$

To further improve the path planner both constants can be optimized using a dynamic system model [10]. Instead of using a pre-calculated value for  $\beta_{ri}$  it is also possible to use a switch condition depending on the traction power. For example, the traction phase can be terminated when the traction power drops to 40% of the average mechanical power in the state FIG\_8. Such a dynamic switch condition is less dependent on the average wind speed or on the aerodynamic characteristics of the kite. Most of these options for improvement are further assessed in [11, 12].

At the end of the upper transition phase the kite is depowered and the set force of the winch changed, which is not shown in Table 15.6.

State	Next state	$\mathbf{p}_{k,set}^{SE}$	$\dot{\chi}_{set}$	Condition
Initial	UP_TURN	—	$\dot{\chi}_{turn}$	always
UP_TURN	UP_FLY_UP	Zenith from PID		$\psi > 360^\circ - \delta\psi \vee \psi < \delta\psi$
UP_FLY_UP	Final	Zenith from PID		$\beta > \beta_{ri}$

**Table 15.6** Finite sub-states of the upper transition phase INT\_UP. An offset of  $\delta\psi \approx 60^\circ$  is needed to compensate for the time delay  $\delta t_{up}$  between the command to stop turning and the kite actually stopping to turn

### 15.3.6 Influence of the Elevation Angle

The planned flight path is depicted in Fig. 15.11 for different set values of the average elevation angle. For the limiting case  $\bar{\beta}_{set} = \beta_{max} = 60^\circ$  the turning points  $C_1$  and  $C_3$  as well as the attractor points  $P_2$  and  $P_4$  coincide, as defined in Sect. 15.3.4. As consequence the states LOW\_TURN and LOW\_LEFT disappear and the kite directly transitions from the retraction into the traction phase.

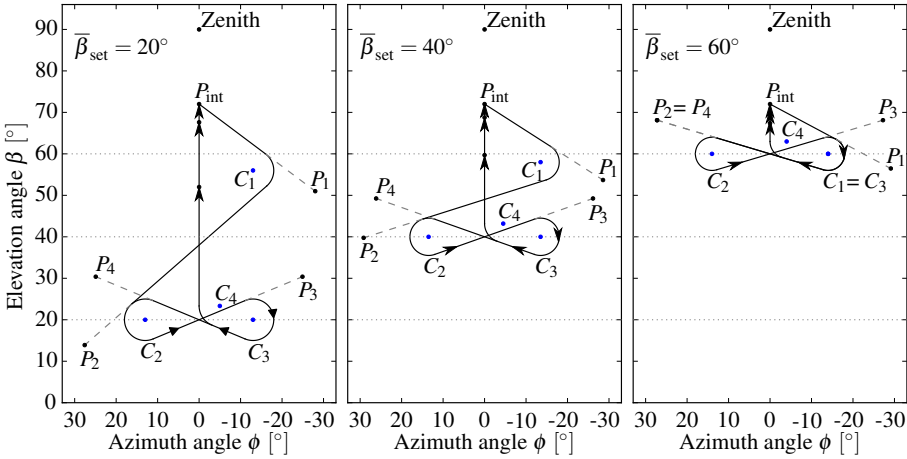


Fig. 15.11 Planned flight path for low, medium and high set values of the average elevation angle

### 15.4 Planning Performance

The performance of the planning approach is first assessed by a dynamic simulation of the 20 kW demonstrator system of Delft University of Technology in a realistic wind environment and subsequently investigated by a quasi-steady analysis.

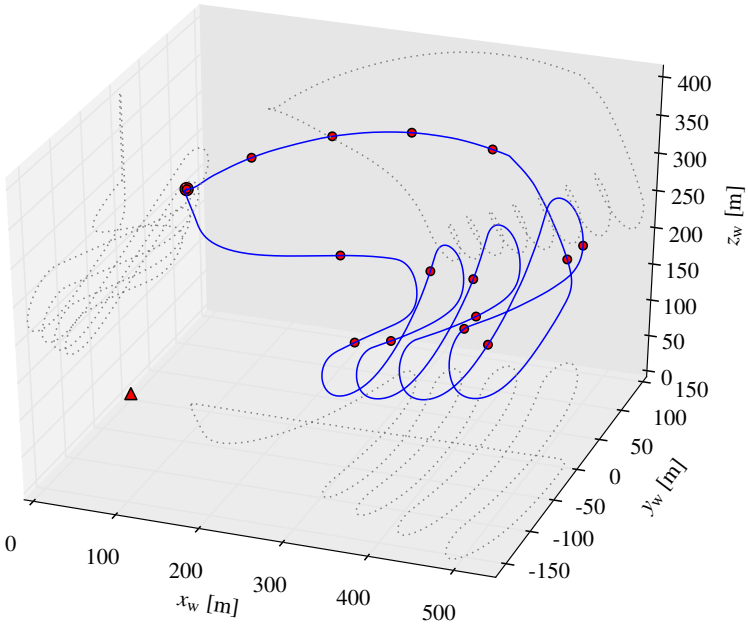
#### 15.4.1 Dynamic System Simulation

The dynamic system model [10] is used with a combination of flight path and winch controllers [11, 12] for simulating pumping cycle operation. The key parameters of the model are listed in Table 15.7. The wind data for the onshore location Cabauw is used, as described in Sect. 15.2.3.

**Table 15.7** Parameters of the simulation model including all relevant system components and accounting for site-specific wind shear profile and turbulent fluctuations

Parameter	Value
Total wing surface area $A_k$ [m <sup>2</sup> ]	25.0
Projected wing surface area $A$ [m <sup>2</sup> ]	20.36
Relative side area $A_{side}/A$ [%]	30.6
Wing mass including sensors $m_k$ [kg]	10.58
Mass of kite control unit $m_{KCU}$ [kg]	11.0
Maximum tether force $F_{t,max}$ [N]	8000.0

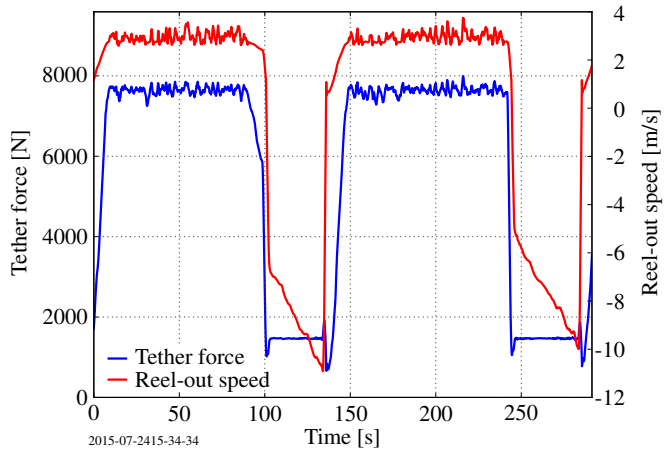
The computed flight path of the kite for a nominal ground wind speed of 6 m/s is shown in Fig. 15.12. The influence of the turbulence intensity  $I_{197} = 7.2\%$  is hardly



**Fig. 15.12** Simulated flight path of the kite at the nominal ground wind speed of 6 m/s. The simulation starts at the enlarged red dot. Smaller dots are placed on the flight path in 10 s intervals. Positions are relative to the ground station which is represented as a red triangle

visible. The corresponding tether force at the ground station and the tether reel-out speed are shown in Fig. 15.13. Figure 15.14 shows the flight path at an increased ground wind speed of 9.2 m/s. The average traction elevation angle  $\beta_{set}$  has been increased to limit the maximum power. Retraction and traction are at nearly the same

**Fig. 15.13** Tether force at the ground and tether reel-out speed for two power cycles at the nominal ground wind speed of 6 m/s. The tether force is close to the maximum value of 8000 N. The reel-out speed is quite constant. Only when the force exceeds the value of 7600 N the upper force controller becomes active and the reel-out speed increases to limit the tether force





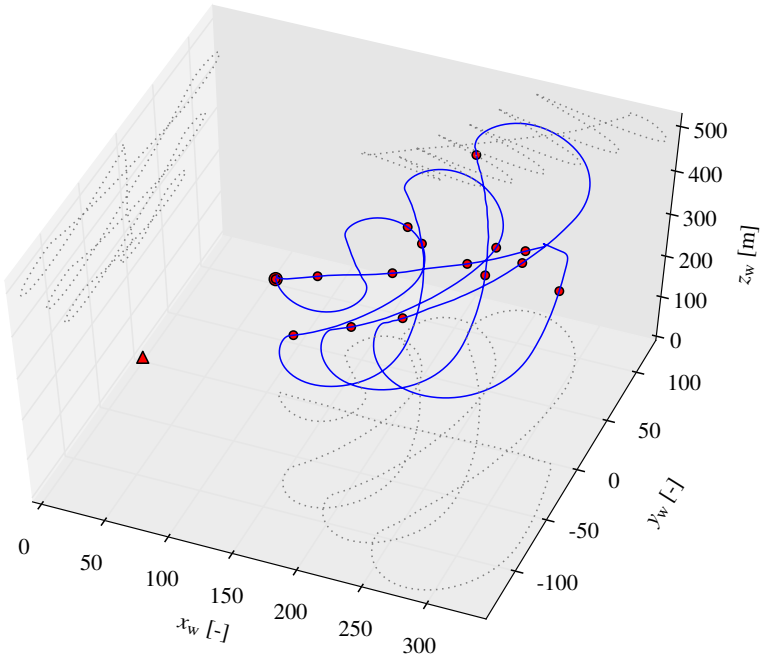
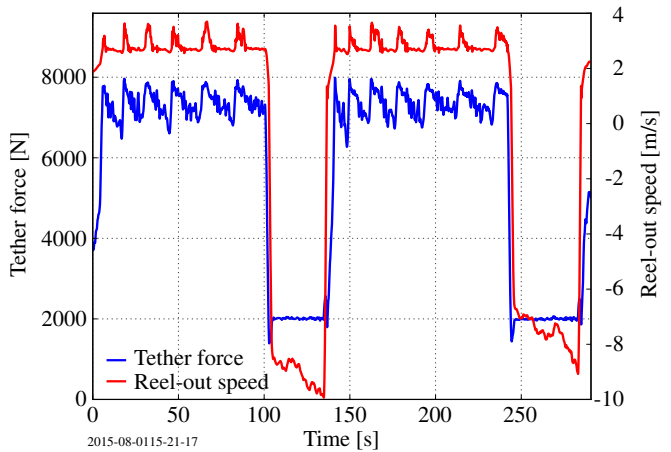


**Fig. 15.14** Simulated flight path of the kite at a higher ground wind speed of 9.2 m/s. The kite is reeled out at an average elevation angle of  $58^\circ$  to limit the maximum power to 30 kW. It is reeled in at about the same elevation angle, skipping the lower transition phase

elevation angle. As a result of the slower retraction phase the cycle time increased to 170 s. The corresponding tether force at the ground station and the reel-out speed are shown in Fig. 15.15.

**Fig. 15.15** Tether force at the ground and reel-out speed for two pumping cycles at a higher ground wind speed of 9.2 m/s. The variations of the force and the reel-out speed are much higher than at lower wind speeds. The reason for this is, that the kite is flying at a high elevation angle and the effective wind speed is strongly varies during the figure eight maneuvers. Nevertheless the traction force and traction power stay within the allowed limits



To achieve these results it was necessary to adapt the depower settings during the traction phase, depending on the elevation angle and the mechanical power. The depower settings are calculated as follows

$$u_d = u_{d,ro} + u_{d,add}K_1 - u_{d,sub}K_2, \quad (15.26)$$

where  $u_{d,ro}$  is a parameter which depends on the estimated wind speed and turbulence intensity. A look-up table is used to obtain this parameter. The values in this look-up table were optimized offline for different combinations of wind speed and turbulence intensities.

Empirically derived values are used for the additional depower contribution  $u_{d,add}$  and the additional power contribution  $u_{d,sub}$ . The integer values  $K_1$  and  $K_2$  depend on the mechanical power, the elevation angle, the turbulence intensity and the ground wind speed.

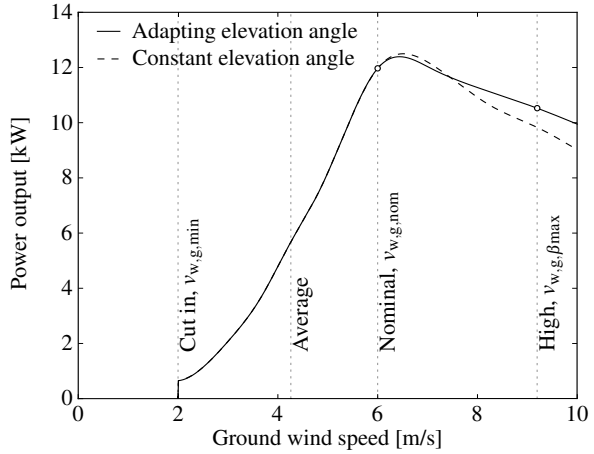
The simulation results are summarized in Table 15.8. The crest factor of the traction force, defined as ratio of the maximum force to the average force in the traction phase, should be close to unity to maximize the power generation of a given system. Further listed are the duty cycle, defined as the ratio of the retraction time to the total cycle time, the pumping efficiency, defined as the ratio of the net mechanical energy to the energy generated in the traction phase, and the cycle efficiency, defined as the ratio of the average mechanical power of the cycle to the average mechanical power during the traction phase. For wind speeds above the nominal wind speed of the simulated system, which is 6 m/s, the traction power increases while the traction power stays constant. Therefore the average power slightly drops.

The computed power curve is shown in Fig. 15.16 demonstrating the advantage of adjusting the average elevation angle during traction compared to just depowering the kite at constant elevation angle.

**Table 15.8** Numerical results for operating the kite described in Table 15.7 at a tether length between 300 and 600 m at ground wind speeds of 6 and 9.2 m/s, respectively. For a detailed definition of the listed parameters see [9]

Ground wind speed	6 m/s	9.2 m/s
Average mechanical power [W]	11953.2	10523.0
Lift to drag ratio, traction [-]	4.97	5.01
Lift to drag ratio, retraction [-]	2.01	1.96
Duty cycle [%]	72.2	73.0
Pumping efficiency [%]	80.1	74.6
Cycle efficiency [%]	57.8	54.5
Crest factor traction power [-]	1.30	1.43
Maximum traction power [W]	27738.2	28781.8
Crest factor traction force [-]	1.08	1.11
Maximum traction force [N]	7899.7	7914.3

**Fig. 15.16** Average mechanical power of a kite power system, using a 20 kW generator with a maximum tether force of 8000 N. Increasing the average elevation angle for larger than nominal wind speeds increases the power output because of the shorter transition phase, but also increases the wear of the de-power actuator. See Figs. 15.6 and 15.7 as references for the available wind resource



### 15.4.2 Quasi-Steady Analysis

Some of the design goals mentioned in Sect. 15.3.1 can be verified on the basis of a quasi-steady modeling framework as described in [9, 23, 25]. Accordingly the analysis presented in the following has the objective to describe the sensitivity of the power output with respect to key problem parameters, such as the average elevation angle  $\bar{\beta}_{set}$  during the traction phase and the exponent  $\alpha$  characterizing the wind speed profile.

To extrapolate the ground wind speed  $v_{w,g}$  to the operating altitude of the kite we use the power law given by Eq. (15.10) with an exponent  $\alpha = 0.234$  to describe the wind resource at Cabauw, the Netherlands. Projecting the wind velocity vector  $\mathbf{v}_w$  at the kite onto the direction vector  $\mathbf{e}_r$  pointing from the ground station to the kite leads to the effective wind speed

$$v_{w,e} = \mathbf{v}_w \cdot \mathbf{e}_r = v_w \cos \beta \cos \phi. \tag{15.27}$$

Combining Eqs. (15.27) and (15.10) and representing the average height as  $\bar{z} = l_t \sin \beta$  we can formulate the dimensionless wind speed gain as

$$\mu = \frac{v_{w,e}}{v_{w,g}} = \cos \beta \cos \phi \left( \frac{l_t \sin \beta}{z_{ref}} \right)^\alpha. \tag{15.28}$$

Based on the quasi-steady theory of tethered flight the normalized tether force for vanishing mass of the airborne system can be evaluated as [23]

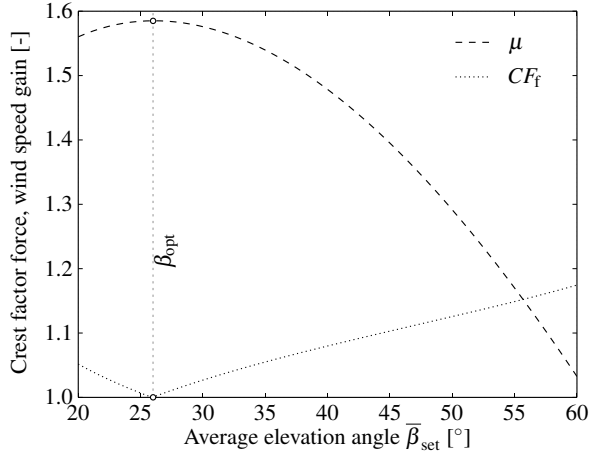
$$\frac{F_t}{q_g S} = C_R \left[ 1 + \left( \frac{L}{D} \right)^2 \right] (\mu^2 - f_g^2), \tag{15.29}$$

where  $q_g = 1/2\rho v_{w,g}^2$  is the dynamic wind pressure at the ground and  $f_g = v_{k,r}/v_{w,g}$  is a nondimensional reeling factor. Accordingly, the crest factor of the traction force can be evaluated for flying figure eight maneuvers at a given tether length and average elevation angle as [9]

$$CF_{f,q} = \left( \frac{\mu_{\max}}{\mu_{\text{av}}} \right)^2. \tag{15.30}$$

The wind speed gain and the crest factor are illustrated in Fig. 15.17 as functions of the average elevation angle  $\bar{\beta}_{\text{set}}$ . At lower elevation angles the wind speed gain can

**Fig. 15.17** The dimensionless wind speed gain  $\mu$  and the crest factor  $CF_f$  of the tether force as functions of the average elevation angle  $\bar{\beta}_{\text{set}}$ . The tether length is  $l_t = 300\text{m}$  and the wind shear exponent is  $\alpha = 0.234$  to approximate the wind speed profile at Cabauw



reach a value of up to 1.53, while the crest factor does not exceed a value of 1.2. Keeping the crest factor below this limit is a design choice: up to this value electrical machines still work efficiently. We find from Fig. 15.17 that the crest factor reaches its minimum of  $CF_f \simeq 1$  at an elevation angle  $\bar{\beta}_{\text{set}} \approx 26^\circ$ .

This minimum is a result of two competing mechanisms. In the lower half of the figure eight maneuver the effective wind speed increases because of a dominating factor  $\cos \beta$ , while in the upper half it increases because of a dominating effect of the wind speed profile. The elevation angle  $\bar{\beta}_{\text{set}} = 26^\circ$  is thus the optimal choice for operating at the nominal wind speed  $v_{w,g,\text{nom}}$  at which the nominal power output is just reached (neglecting the tether drag within the scope of this analysis). Figure 15.18 quantifies how the optimal elevation angle  $\beta_{\text{opt}}$  varies as a function of the wind shear exponent  $\alpha$ .

As discussed in the context of Fig. 15.16 the tether force in the traction phase reaches its maximum value  $F_{t,\text{max}}$  for the nominal wind speed  $v_{w,g,\text{nom}}$ . For higher wind speeds the tether force can efficiently be limited to  $F_{t,\text{max}}$  by increasing the average elevation angle  $\bar{\beta}_{\text{set}}$  without the need to additionally depower the wing. This planning strategy can be used until the maximum elevation angle  $\beta_{\text{max}}$  is reached. For even higher wind speeds the kite must additionally be depowered to keep the tether force during the traction phase below  $F_{t,\text{max}}$ .

To determine this threshold wind speed, which is an operational characteristic of the system, we define the velocity ratio

$$v = \frac{\mu_{av,max}}{\mu_{av,min}}, \tag{15.31}$$

where  $\mu_{av,max}$  is the average wind speed gain at  $\bar{\beta}_{set} = \beta_{opt}$  and  $\mu_{av,min}$  is the average wind speed gain at  $\bar{\beta}_{set} = \beta_{max}$ . The ratio  $v$  and the optimum elevation angle  $\beta_{opt}$  are depicted in Fig. 15.18 as functions of the wind shear exponent. Given its definition

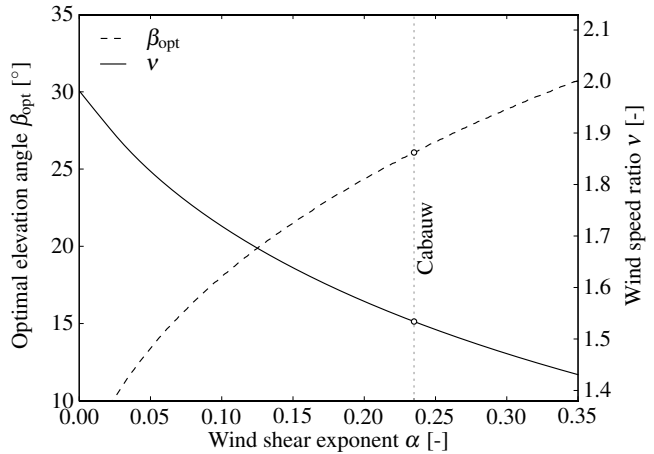


**Fig. 15.18** Optimal elevation angle  $\beta_{opt}$  and wind speed ratio  $v$  both as functions of the wind shear exponent  $\alpha$ . For a uniform wind field ( $\alpha = 0$ ) a value of  $v = 1.98$  can be achieved by adjusting the average elevation angle to  $\beta_{max}$ . For the wind speed profile at Cabauw ( $\alpha = 0.234$ ) a value of  $v = 1.53$  is achievable

by Eq. (15.31) the wind speed ratio  $v$  can be used in two different ways. For a specific fixed ground wind speed  $v_{w,g}$  it quantifies the ratio of the effective wind speeds at nominal operation with  $\beta_{opt}$  and at operation with maximum elevation angle  $\beta_{max}$ . Alternatively,  $v$  quantifies the ratio of the maximum ground wind speed  $v_{w,g,\beta_{max}}$  at which the system can be operated at  $\beta_{max}$ , without additionally depowering the wing during traction, and the nominal ground wind speed  $v_{w,g,nom}$  for operation with  $\beta_{opt}$ . Both interpretations follow from the definitions by Eqs. (15.28) and (15.31).

For the wind speed profile in Cabauw we find from Fig. 15.18 a ratio of  $v = 1.53$ . From this we derive that for a nominal ground wind speed  $v_{w,g,nom} = 6$  m/s the system can be operated up to a ground wind speed of  $v_{w,g,\beta_{max}} = 9.2$  m/s without increasing the depower settings during traction, assuming a negligible turbulence. According to the measured wind speed distribution displayed in Fig. 15.3 this means that when neglecting turbulence, in total about 96% of the time it is not necessary to change the angle of attack of the wing to limit the maximum power.

## 15.5 Conclusions and Outlook

This chapter comprises three distinct contributions. Firstly, we investigate the physics of tethered flight in a realistic wind environment with a particular focus the steering and depowering of a flexible membrane wing by a suspended cable robot as well as on the modeling of wind shear and turbulence. Introducing spherical coordinates we separate the radial motion, managed by the winch controller, from the tangential motion, managed by the flight path controller. We derive the kinematic relations describing straight flight along great circle segments as well as turning flight with constant radius, along small circle segments. These path segments are used to compose an entire pumping cycle, consisting of figure eight flight maneuvers during the traction phase and retraction and transition maneuvers to close the cycle. The effect of gravity on the flight dynamics during straight and turning flight is shown qualitatively by photographic data.

As a second contribution a flight path planning scheme for automatic power generation in pumping cycles is presented. The path is described in the plane spanned by the azimuth and elevation angles by a concise set of parameters: the width  $w_{\text{fig}}$ , height  $h_{\text{fig}}$  and average elevation angle  $\bar{\beta}_{\text{set}}$  of the figure eight flight maneuvers, the elevation angle  $\beta_{\text{ri}}$  for starting the depower phase and the minimum attractor point distance  $\delta_{\text{min}}$ . To reduce the power fluctuations at higher elevation angles the height of the figure eight is decreased linearly with increasing  $\bar{\beta}_{\text{set}}$ . To compensate the steering delay we propose to use three empiric parameters,  $\delta\chi$ ,  $\delta\chi_{\text{int}}$  and  $\delta\psi$ , which are tuned manually to minimize the error between the planned and the actual flight paths.

The third contribution of the chapter is a performance assessment and sensitivity analysis of the planning scheme. To assess the performance we numerically simulate the pumping operation in a realistic turbulent wind environment. Using a dynamic model of the kite power system in conjunction with the Mann turbulence model we consider nominal operation at a ground wind speed of 6 m/s and operation at a higher wind speed of 9.2 m/s. Within this speed range the generated power can be kept nearly constant by adjusting the average elevation angle  $\bar{\beta}_{\text{set}}$  during traction. This force control strategy has proven to be more effective than just depowering the kite in the traction phase. Based on a quasi-steady analysis we demonstrated that increasing  $\bar{\beta}_{\text{set}}$  up to a maximum value of  $\beta_{\text{max}} = 60^\circ$  significantly reduces the loss of efficiency above the nominal wind speed. It does however require a higher level of activity of the depower actuator.

Although a first important step has been achieved the flight path can be optimized further. The current system model predicts a maximum average power output for a minimum width  $w_{\text{fig}}$  of the figure eight maneuver. It is clear though that this does not correspond to reality because the steering-induced aerodynamic drag has been neglected in the model. Based on our experiences from test flights a good compromise between maximum power output and high robustness towards sensor errors is achieved by a value of  $w_{\text{fig}} = 36^\circ$ . Extending the flight path planner to a control scheme that allows retraction of the kite at the side of the wind window is also a

future goal. This might improve the power output particularly for deployment scenarios with low-altitude limit.

**Acknowledgements** The financial support of the European Commission through the projects AWESCO (H2020-ITN-642682) and REACH (H2020-FTIPilot-691173) is gratefully acknowledged.

## References

1. Archer, C. L., Jacobson, M. Z.: Evaluation of global wind power. *Journal of Geophysical Research: Atmospheres* **110**(D12), 1–20 (2005). doi: [10.1029/2004JD005462](https://doi.org/10.1029/2004JD005462)
2. Baayen, J. H., Ockels, W. J.: Tracking control with adaption of kites. *IET Control Theory and Applications* **6**(2), 182–191 (2012). doi: [10.1049/iet-cta.2011.0037](https://doi.org/10.1049/iet-cta.2011.0037)
3. Bosch, A., Schmehl, R., Tiso, P., Rixen, D.: Dynamic nonlinear aeroelastic model of a kite for power generation. *AIAA Journal of Guidance, Control and Dynamics* **37**(5), 1426–1436 (2014). doi: [10.2514/1.G000545](https://doi.org/10.2514/1.G000545)
4. Breukels, J.: An Engineering Methodology for Kite Design. Ph.D. Thesis, Delft University of Technology, 2011. <http://resolver.tudelft.nl/uuid:cdece38a-1f13-47cc-b277-ed64fdda7cdf>
5. Cherubini, A., Papini, A., Verthey, R., Fontana, M.: Airborne Wind Energy Systems: A review of the technologies. *Renewable and Sustainable Energy Reviews* **51**, 1461–1476 (2015). doi: [10.1016/j.rser.2015.07.053](https://doi.org/10.1016/j.rser.2015.07.053)
6. Erhard, M., Strauch, H.: Theory and Experimental Validation of a Simple Comprehensible Model of Tethered Kite Dynamics Used for Controller Design. In: Ahrens, U., Diehl, M., Schmehl, R. (eds.) *Airborne Wind Energy, Green Energy and Technology*, Chap. 8, pp. 141–165. Springer, Berlin Heidelberg (2013). doi: [10.1007/978-3-642-39965-7\\_8](https://doi.org/10.1007/978-3-642-39965-7_8)
7. Erhard, M., Strauch, H.: Control of Towing Kites for Seagoing Vessels. *IEEE Transactions on Control Systems Technology* **21**(5), 1629–1640 (2013). doi: [10.1109/TCST.2012.2221093](https://doi.org/10.1109/TCST.2012.2221093)
8. Fagiano, L., Zraggen, A. U., Morari, M., Khammash, M.: Automatic crosswind flight of tethered wings for airborne wind energy: modeling, control design and experimental results. *IEEE Transactions on Control System Technology* **22**(4), 1433–1447 (2014). doi: [10.1109/TCST.2013.2279592](https://doi.org/10.1109/TCST.2013.2279592)
9. Fechner, U., Schmehl, R.: Model-Based Efficiency Analysis of Wind Power Conversion by a Pumping Kite Power System. In: Ahrens, U., Diehl, M., Schmehl, R. (eds.) *Airborne Wind Energy, Green Energy and Technology*, Chap. 14, pp. 249–269. Springer, Berlin Heidelberg (2013). doi: [10.1007/978-3-642-39965-7\\_14](https://doi.org/10.1007/978-3-642-39965-7_14)
10. Fechner, U., Vlught, R. van der, Schreuder, E., Schmehl, R.: Dynamic Model of a Pumping Kite Power System. *Renewable Energy* (2015). doi: [10.1016/j.renene.2015.04.028](https://doi.org/10.1016/j.renene.2015.04.028). [arXiv:1406.6218 \[cs.SY\]](https://arxiv.org/abs/1406.6218)
11. Fechner, U.: A Methodology for the Design of Kite-Power Control Systems. Ph.D. Thesis, Delft University of Technology, 2016. doi: [10.4233/uuid:85efaf4c-9dce-4111-bc91-7171b9da4b77](https://doi.org/10.4233/uuid:85efaf4c-9dce-4111-bc91-7171b9da4b77)
12. Fechner, U., Schmehl, R.: Flight Path Control of Kite Power Systems in a Turbulent Wind Environment. In: *Proceedings of the 2016 American Control Conference (ACC)*, pp. 4083–4088, Boston, MA, USA, 6–8 July 2016. doi: [10.1109/ACC.2016.7525563](https://doi.org/10.1109/ACC.2016.7525563)
13. Fechner, U., Schmehl, R.: Flight Path Planning in a Turbulent Wind Environment. In: Schmehl, R. (ed.) *Book of Abstracts of the International Airborne Wind Energy Conference 2015*, pp. 56–57, Delft, The Netherlands, 15–16 June 2015. doi: [10.4233/uuid:7df59b79-2c6b-4e30-bd58-8454f493bb09](https://doi.org/10.4233/uuid:7df59b79-2c6b-4e30-bd58-8454f493bb09). Presentation video recording available from: <https://collegerama.tudelft.nl/Mediasite/Play/0856a922984242c58bd46c84db3d320f1d>

14. Gros, S., Zanon, M., Diehl, M.: A relaxation strategy for the optimization of Airborne Wind Energy systems. In: Proceedings of the 2013 European Control Conference (ECC), pp. 1011–1016, Zurich, Switzerland, 17–19 July 2013
15. Horn, G., Gros, S., Diehl, M.: Numerical Trajectory Optimization for Airborne Wind Energy Systems Described by High Fidelity Aircraft Models. In: Ahrens, U., Diehl, M., Schmehl, R. (eds.) *Airborne Wind Energy, Green Energy and Technology*, Chap. 11, pp. 205–218. Springer, Berlin Heidelberg (2013). doi: [10.1007/978-3-642-39965-7\\_11](https://doi.org/10.1007/978-3-642-39965-7_11)
16. International Electrotechnical Commission: Power performance measurements of electricity producing wind turbines, IEC Standard 61400-12-1:2005(E)
17. Jehle, C.: Automatic Flight Control of Tethered Kites for Power Generation. M.Sc.Thesis, Technical University of Munich, Germany, 2012. <https://mediatum.ub.tum.de/doc/1185997/1185997.pdf>
18. Jehle, C., Schmehl, R.: Applied Tracking Control for Kite Power Systems. *AIAA Journal of Guidance, Control, and Dynamics* **37**(4), 1211–1222 (2014). doi: [10.2514/1.62380](https://doi.org/10.2514/1.62380)
19. Mann, J.: The spatial structure of neutral atmospheric surface-layer turbulence. *Journal of Fluid Mechanics* **273**, 141 (1994). doi: [10.1017/S0022112094001886](https://doi.org/10.1017/S0022112094001886)
20. Mann, J.: Wind field simulation. *Probabilistic Engineering Mechanics* **13**(4), 269–282 (1998). doi: [10.1016/S0266-8920\(97\)00036-2](https://doi.org/10.1016/S0266-8920(97)00036-2)
21. Ruiterkamp, R., Sieberling, S.: Description and Preliminary Test Results of a Six Degrees of Freedom Rigid Wing Pumping System. In: Ahrens, U., Diehl, M., Schmehl, R. (eds.) *Airborne Wind Energy, Green Energy and Technology*, Chap. 26, pp. 443–458. Springer, Berlin Heidelberg (2013). doi: [10.1007/978-3-642-39965-7\\_26](https://doi.org/10.1007/978-3-642-39965-7_26)
22. Schmehl, R., Vlugt, R. van der, Fechner, U., Wachter, A. de, Ockels, W.: Airborne Wind Energy System. Dutch Patent Application 2,009,528, Mar 2014
23. Schmehl, R., Noom, M., Vlugt, R. van der: Traction Power Generation with Tethered Wings. In: Ahrens, U., Diehl, M., Schmehl, R. (eds.) *Airborne Wind Energy, Green Energy and Technology*, Chap. 2, pp. 23–45. Springer, Berlin Heidelberg (2013). doi: [10.1007/978-3-642-39965-7\\_2](https://doi.org/10.1007/978-3-642-39965-7_2)
24. The Royal Netherlands Meteorological Institute (KNMI): Cabauw Tower Meteorological Profiles. CESAR Database. <http://www.cesar-database.nl> (2011). Accessed 30 May 2016
25. Vlugt, R. van der, Bley, A., Schmehl, R., Noom, M.: Quasi-Steady Model of a Pumping Kite Power System. Submitted to *Renewable Energy* (2017). [arXiv:1705.04133 \[cs.SY\]](https://arxiv.org/abs/1705.04133)
26. Vlugt, R. van der, Peschel, J., Schmehl, R.: Design and Experimental Characterization of a Pumping Kite Power System. In: Ahrens, U., Diehl, M., Schmehl, R. (eds.) *Airborne Wind Energy, Green Energy and Technology*, Chap. 23, pp. 403–425. Springer, Berlin Heidelberg (2013). doi: [10.1007/978-3-642-39965-7\\_23](https://doi.org/10.1007/978-3-642-39965-7_23)
27. Zraggen, A. U., Fagiano, L., Morari, M.: Automatic Retraction and Full-Cycle Operation for a Class of Airborne Wind Energy Generators. *IEEE Transactions on Control Systems Technology* **24**(2), 594–608 (2015). doi: [10.1109/TCST.2015.2452230](https://doi.org/10.1109/TCST.2015.2452230)
28. Zraggen, A. U., Fagiano, L., Morari, M.: Automatic Retraction Phase of Airborne Wind Energy Systems. Proceedings of the 19th IFAC World Congress **47**(3), 5826–5831 (2014). doi: [10.3182/20140824-6-ZA-1003.00624](https://doi.org/10.3182/20140824-6-ZA-1003.00624)
29. Zraggen, A. U., Fagiano, L., Morari, M.: On real-time optimization of airborne wind energy generators. In: Proceedings of the 52nd IEEE Conference on Decision and Control, pp. 385–390, IEEE, Firenze, Italy, 10–13 Dec 2013. doi: [10.1109/CDC.2013.6759912](https://doi.org/10.1109/CDC.2013.6759912)
30. Zraggen, A. U., Fagiano, L., Morari, M.: Real-Time Optimization and Adaptation of the Crosswind Flight of Tethered Wings for Airborne Wind Energy. *IEEE Transactions on Control Systems Technology* **23**(2), 434–448 (2015). doi: [10.1109/TCST.2014.2332537](https://doi.org/10.1109/TCST.2014.2332537)